



Hot forging of Mg–4Al–2Ba–2Ca (ABaX422) alloy and validation of processing map

K. SURESH¹, K. P. RAO¹, Y. V. R. K. PRASAD², N. HORT³, H. DIERINGA³

1. Department of Mechanical and Biomedical Engineering, City University of Hong Kong, Tat Chee Avenue, Kowloon, Hong Kong, China;
2. Processingmaps.com No. 2/B, Vinayaka Nagar, Hebbal, Bengaluru 560024, India;
3. Helmholtz-Zentrum Geesthacht, Institute of Materials Research, Magnesium Innovation Centre, Max-Planck-Straße 1, Geesthacht 21502, Germany

Received 8 September 2017; accepted 28 January 2018

Abstract: A cup-shaped component of Mg–4Al–2Ba–2Ca (ABaX422) alloy was forged in the temperature range of 300–500 °C and at speeds in the range of 0.01–10 mm/s with a view to validate the processing map and study the microstructural development. The process was simulated through finite-element method to estimate the local and average strain rate ranges in the forging envelope. The processing map exhibited two domains in the following ranges: (1) 300–390 °C and 0.0003–0.001 s⁻¹, and (2) 400–500 °C and 0.0003–0.3 s⁻¹ and both represented dynamic recrystallization (DRX). The map revealed a wide flow instability regime at higher strain rates and temperatures lower than 400 °C, in which flow localization occurred. Forgings produced under conditions of the above two domains were sound and symmetrical, and had finer grain sizes when being forged in the first domain. However, when being forged in the flow instability regimes, the alloy fractured before the final shape was reached. The experimental load–stroke curves for the conditions within the domains correlated well with the simulated ones, whereas the curves obtained in the instability regime were uneven.

Key words: magnesium alloy; processing map; hot forging; dynamic recrystallization

1 Introduction

In recent years, magnesium alloys are being developed for aerospace, automobile, and biomedical applications due to their lightweight. One of the most popular series of alloys is based on Mg–Al–Zn system because both Al and Zn dissolve in Mg and cause solid solution strengthening [1,2]. The strength, ductility, and creep resistance may be improved further by alloying with rare-earth elements [3–5], which are expensive. The creep resistance may also be improved by the addition of relatively cheaper alkaline-earth elements like Ca, Sr and Ba [6–8] since these elements form stable intermetallic particles in the matrix, which cause dispersion strengthening. In general, a combination of these elements is considered to give better effect as is found [7] for example in MRI230D alloy that contains 7% Al, 2.1% Ca, and 0.3% Sr (mass fraction), where three different thermally stable intermetallic phases Al₄Sr,

Mg₂Ca and (Mg,Al)₂Ca form in the matrix [9]. However, Sr addition is not favored because of its detrimental effect on the corrosion resistance of several magnesium alloys [10]. Addition of Ba to AZ91 alloy resulted in higher temperature strength and increased ignition temperature [8]. When Ba is added along with Ca, it forms a eutectic phase Mg₁₇Ba₂ and a tertiary compound (Al,Mg)₂Ca at the grain boundaries, preventing their sliding during creep deformation [11]. These findings formed the basis for the recent development of two creep resistant alloys Mg–4Al–2Ba–1Ca (ABaX421) and Mg–4Al–2Ba–2Ca (ABaX422), which had better creep resistance than Mg–4Al–2RE (AE42) and Mg–3Sn–2Ca (TX32) alloys [7]. The strength of ABaX422 [12] is better than that of AZ31 and AZX312 alloys in the temperature range of 25–250 °C. The hot working behavior of ABaX422 has been studied [12] using processing map and the alloy offers two workability domains, a higher temperature one for bulk working and a lower temperature one for grain refinement.

In general, magnesium alloys have limited workability at low temperatures because of the limited number of operative slip systems, mainly basal slip. As the temperature is increased, some contribution from prismatic slip occurs to satisfy the necessity of five independent slip systems for continuity of deformation across the grains. Bulk metal forming operations involve large plastic deformation and require high temperatures to activate additional non-basal slip systems, like pyramidal slip, to contribute to deformation of such alloys. The hot workability depends on the alloy chemistry, starting microstructure, inhomogeneity, grain size and the state-of-stress in the forming process. The process of dynamic recrystallization (DRX) is essential for breaking the as-cast microstructure and refining the grain size. DRX involves nucleation and grain boundary migration involving the generation of dislocations as well as their recovery through climb or cross-slip. The climb process is the main recovery mechanism when plastic deformation is mainly due to basal slip and/or prismatic slip while cross-slip is the mechanism for recovery process for pyramidal slip [13,14].

The aim of the present work is to forge the alloy to form a cup-shape component, in accordance with the findings of the processing map, and validate its results on the formability and microstructural development. The methodology is similar to that applied earlier to validate the processing maps on electrolytic copper [15] and rolled AZ31alloy [16–18], which essentially consists of process simulation using finite element method (FEM) and controlled forging experiments using die and punch on MTS-servo hydraulic machine.

2 Methodology

2.1 Processing map development

The processing map for a material is developed based on its flow stress as a function of temperature and strain rate. The detailed principles and procedures have been described earlier, including maps for a large number of magnesium alloys [19,20]. The efficiency of power dissipation occurring through microstructural changes during deformation is given by

$$\eta = 2m/(m+1) \quad (1)$$

where m is the strain rate sensitivity of flow stress. A three-dimensional plot of efficiency variation with temperature and strain rate gives a power dissipation map, which may be viewed as a contour map drawn with iso-efficiency contours.

Flow instability criterion is derived by exploring the extremum principles of irreversible thermodynamics as applied to continuum mechanics of large plastic flow [21], which is given by instability parameter $\xi(\dot{\epsilon})$:

$$\xi(\dot{\epsilon}) = \frac{\partial \ln[m/(m+1)]}{\partial \ln \dot{\epsilon}} + m \leq 0 \quad (2)$$

The variation of $\xi(\dot{\epsilon})$ with temperature and strain rate gives the instability map, which may be superimposed on the power dissipation map for obtaining a processing map. The map is conveniently viewed as a contour map, where isoefficiency contours are drawn on a frame of temperature and strain rate (logarithmic scale). Accurate experimental data of flow stress as a function of temperature and strain rate, in a wide range, are required to generate the processing map, the procedure for which was explained earlier [19]. The processing map reveals domains, where different microstructural mechanisms like dynamic recrystallization (DRX) operate along with the limiting conditions for regimes where flow instability occurs.

2.2 FEM simulation model

The FEM model used in this work is the DEFORM program, which is a code developed based on a rigid viscoplastic model using the principle of analysis of large plastic incremental deformation (ALPID) by KOBAYASHI et al [22]. The basis for the FEM simulation program has been presented by OH [23]. Briefly, FEM uses extremum principles, which state that for a plastically deforming body of volume, V , under the traction, \mathbf{F} , prescribed on a part of the surface, S_F , and the velocity, \mathbf{u} , prescribed on the surface, S_U , it uses variational principles in minimizing the function:

$$\phi = \int \bar{\sigma} \bar{\epsilon} dV - \int \frac{\alpha}{2} (\dot{\epsilon}_v)^2 dV - \int \mathbf{F} \cdot \mathbf{u} dS \quad (3)$$

where $\dot{\epsilon}$ is the effective strain rate, $\bar{\sigma}$ is the effective stress, $\bar{\epsilon}$ is the effective strain, \mathbf{u} is the velocity vector, $\dot{\epsilon}_v$ is the volumetric strain rate, and α is a large positive constant (penalty). The program accepts constitutive equation data, the geometry of the die and punch, and the friction coefficient. The program also has an automatic remeshing option when the finite element mesh distorts and the nodes meet (Jacobian goes negative). The relevant output of the simulation model consists of the local values of stress, strain, strain rate and velocity vectors. In addition, the load–stroke curves can be obtained for each forging simulation.

3 Experimental

The magnesium alloy Mg–4Al–2Ba–2Ca (ABaX422) billet was prepared by conventional casting method using elemental metals. While the molten Mg–4Al alloy was kept at 720 °C under SF₆–argon mix cover gas, Ca and Ba were added. The melt was held at the same temperature for another 5 min before being poured in a preheated permanent steel mold. A cast billet

with 100 mm in diameter obtained using the above procedure was diametrically sliced into disks. Slugs with 12.5 mm in diameter and 14 mm in height were machined for forging tests. One end of the slug was chamfered for specimen aligning and centering on the forging die.

Isothermal forging experiments were conducted on cylindrical specimens of the geometry shown in Fig. 1(a) to produce a rib-web (cup) shape shown in Fig. 1(b). The load train assembly is shown in Fig. 1(c). The experiments were conducted at different temperatures in the range of 300–500 °C (in steps of 40 °C) and at speeds of 0.01, 0.1, 1.0 and 10 mm/s using MTS 810 servo-hydraulic machine. These parameters were chosen such that the workability domain, as well as instability regimes, is covered for validation. Details of the test set-up and procedure have been described in earlier publications [15–18].

The procedure involved heating the die and punch to the testing temperature before loading the specimen on the die. Before the experiment, the specimen was lubricated with a grease paste containing graphite and

heated for 15 min. However, during deformation, contact surface friction had no influence on the metallurgical structure development. As the tapered punch pierced the material, the latter flowed opposite the punch, wrapping around the punch and producing a cup-shape at the end of the stroke, which was limited to about 11 mm. The load–stroke curve was recorded in each experiment. The forged specimens were quenched in water and prepared for microstructural examination by sectioning the deformed specimens at the center, parallel to the compression axis. The cut surface was mounted, polished, and etched with a picric acid solution. An optical microscope (OLYMPUS/PMG3) was used to record the microstructure in the rib regions where strains were significant but gradients were smaller.

4 Results and discussion

4.1 Initial microstructure

The as-cast microstructure of ABaX422 alloy is shown as an optical micrograph in Fig. 2(a). The average grain size is about 25 μm, which indicates that the grain

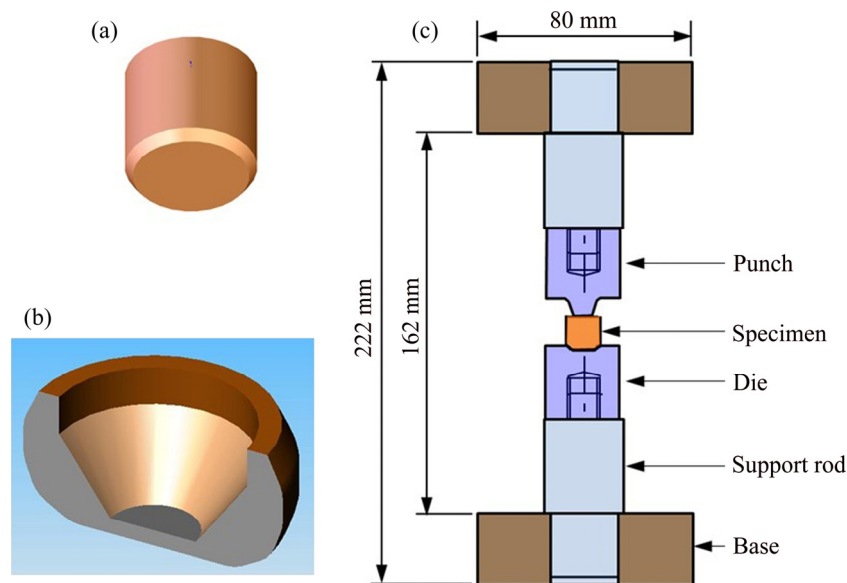


Fig. 1 Sketches of starting specimen (a), final shape of forging (b) and design of load train assembly for forging using servo-hydraulic machine (c) [16]

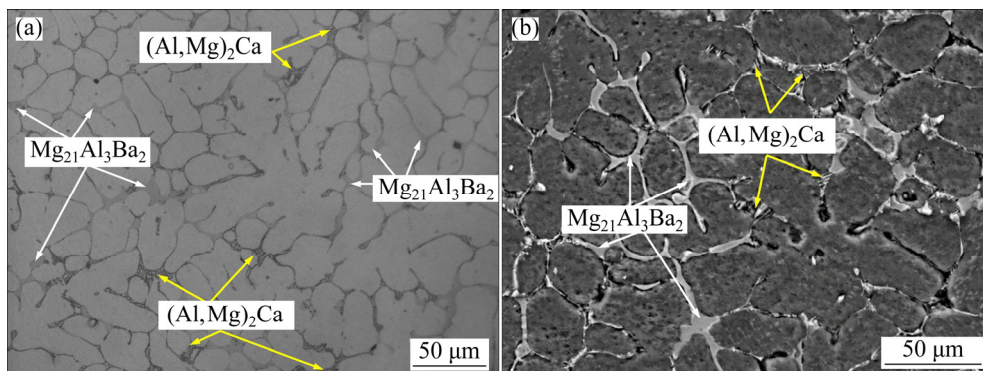


Fig. 2 Optical microstructure (a) and SEM micrograph (b) of as-cast Mg-4Al-2Ba-2Ca alloy

size is considerably refined, compared with grain sizes of 200–500 μm generally observed in other as-cast Mg alloys [24]. Scanning electron microscopy and energy dispersive spectroscopy analysis has revealed that $\text{Mg}_{21}\text{Al}_3\text{Ba}_2$ and $(\text{Al},\text{Mg})_2\text{Ca}$ phases are present at the grain boundaries (Fig. 2(b)).

4.2 Processing map and its interpretation

Details of the processing map obtained on ABaX422 alloy and interpretation of the domains, in terms of microstructural mechanisms, are given in earlier publications [12,25]. For the purpose of ready reference, the processing map obtained at a strain of 0.5 is shown in Fig. 3. The numbers marked on the contours represent efficiency of power dissipation expressed in percent. The shaded areas represent the regimes of flow instability. The map exhibits two domains as described below:

1) Domain 1 occurs in the temperature range of 300–390 $^{\circ}\text{C}$ and strain rate range of 0.0003–0.001 s^{-1} with a peak efficiency of 36% occurring at 340 $^{\circ}\text{C}$ and 0.0003 s^{-1} .

2) Domain 2 occurs in the temperature range of 400–500 $^{\circ}\text{C}$ and strain rate range of 0.0003–0.3 s^{-1} with a peak efficiency of 41% occurring at 500 $^{\circ}\text{C}$ and 0.0003 s^{-1} .

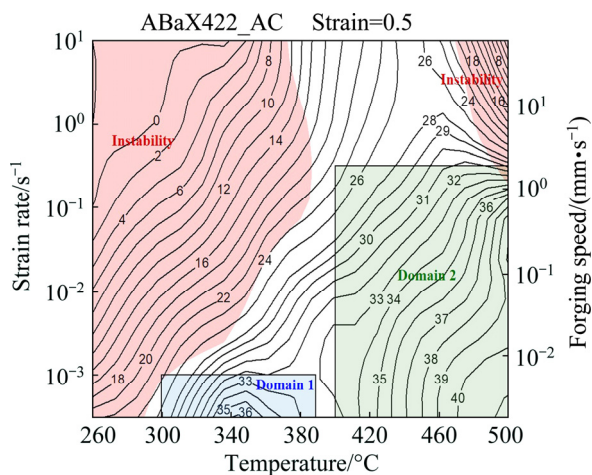


Fig. 3 Processing map for as-cast Mg–4Al–2Ba–2Ca alloy at strain of 0.5 (The numbers associated with the contours indicate efficiency of power dissipation in percent and the shaded areas indicate the instability area)

The changeover has occurred at about 390 $^{\circ}\text{C}$. Based on the microstructural observations, the two domains are interpreted to represent dynamic recrystallization (DRX), which replaces the as-cast microstructure with a wrought equiaxed grain structure. The grain size is finer in Domain 1 than in Domain 2. In the first domain, basal + prismatic slip causes the plastic flow and simultaneous recovery occurs by climb process. In the second domain, which is at higher temperatures,

second order pyramidal slip occurs with simultaneous recovery by cross-slip process. Flow instability occurs mostly at lower temperatures and higher strain rates (grey color shaded area in Fig. 3), and its microstructural manifestation is through flow localization.

4.3 Process simulation

The process simulation based on FEM has become an effective tool in flow investigation during material forming, as demonstrated by SIVAPRASAD et al [26] for optimizing the extrusion of a stainless steel, by OU et al [27] for the forging of aerofoils using a nickel alloy, and by JIN et al [28] for the forging of spur gear using AZ31 magnesium alloy. Such simulations provide information on the flow pattern during die filling as well as on the local values of state-of-stress, strain, and strain rate. These values may be used in predicting the microstructural developments. This model also predicts the forging loads so that the required forging equipment capacity may be determined [22]. A finite element simulation of the forging process was conducted under isothermal conditions (the work-piece and the die remained under the same temperature) using the software DEFORM 2D axisymmetric version equipped with a pre-processor to input material data and object definition. A post-processor was also used, which provides information on deformed geometry, state-of-stress, velocity vectors, strain and strain rate.

Process simulations were conducted in the temperature range of 300–500 $^{\circ}\text{C}$ at speeds from 0.01 to 10 mm/s until the stroke reached 11 mm in 0.1 mm increments. As an example, the effective strain distributions in the forged component at the end of the stroke are shown in Figs. 4(a) and 4(b) for forgings corresponding to 340 $^{\circ}\text{C}$, 0.01 mm/s (Domain 1) and 460 $^{\circ}\text{C}$, 0.01 mm/s (near peak conditions in Domain 2), respectively. From the simulations, the minimum and maximum effective strains range between 0.1 and 3.8. The average strain rates corresponding to the forging speeds of 0.01, 0.1, 1.0 and 10 mm/s are 0.001, 0.01, 0.1 and 1.0 s^{-1} , respectively. The simulations done at 300 $^{\circ}\text{C}$ and at a forging speed of 1 mm/s and, 500 $^{\circ}\text{C}$ and 10 mm/s are shown in Figs. 5(a) and 5(b), respectively, and these two conditions correspond to the two flow instability regimes of the processing map (Fig. 3). The flow patterns are not significantly different from those shown in Fig. 4.

4.4 Microstructural correlation

The microstructures recorded at various locations of the specimens forged at temperatures and speeds of 340 $^{\circ}\text{C}$, 0.01 mm/s (Domain 1) and 460 $^{\circ}\text{C}$, 0.01 mm/s (Domain 2) are shown in Figs. 6(a) and 6(b), respectively. These microstructures recorded in the bottom region of

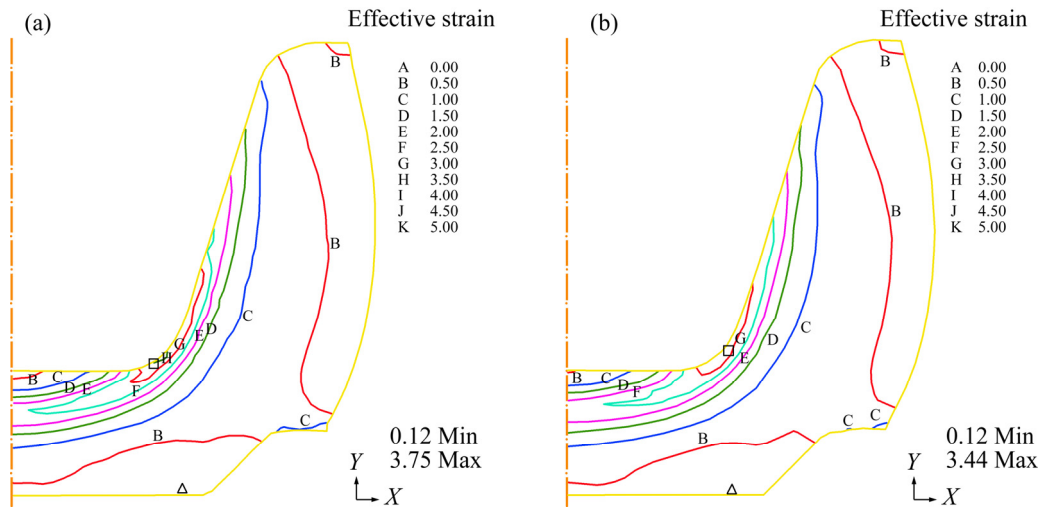


Fig. 4 Strain contours obtained in finite element simulation at end of stroke (11 mm) obtained at temperature and speed corresponding to Domain 1 and Domain 2: (a) 340 °C, 0.01 mm/s (Domain 1); (b) 460 °C, 0.01 mm/s (Domain 2)

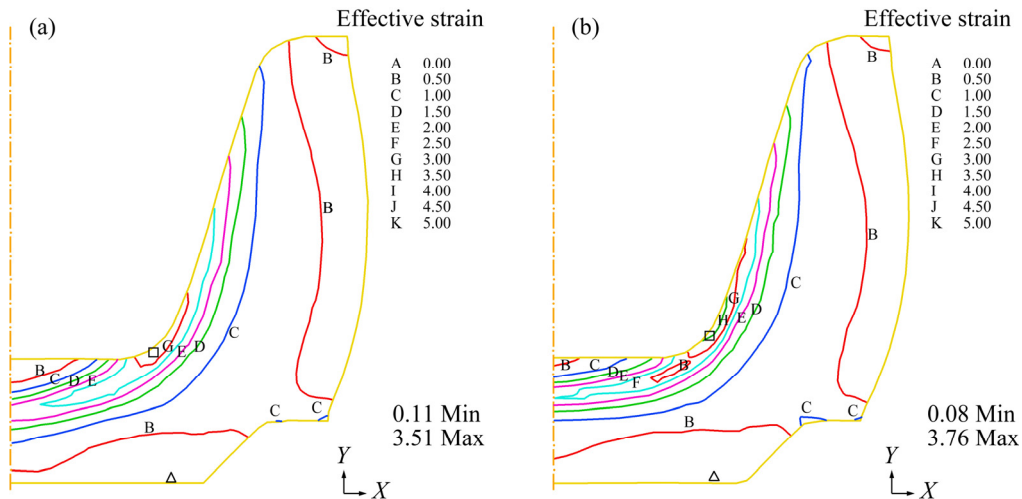


Fig. 5 Strain contours obtained in finite element simulation at end of stroke (11 mm) obtained at temperature and speed corresponding to instability regimes: (a) 300 °C, 1 mm/s; (b) 500 °C, 10 mm/s

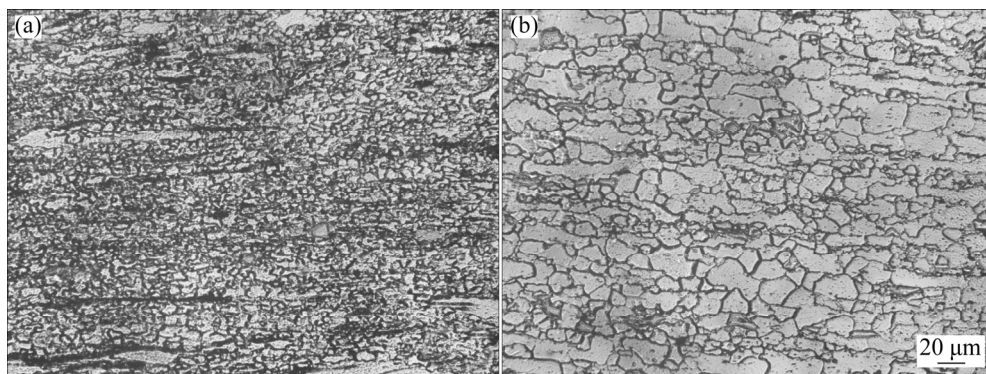


Fig. 6 Microstructures of Mg-4Al-2Ba-2Ca specimens forged at different temperatures and speeds: (a) 340 °C, 0.01 mm/s (Domain 1); (b) 460 °C, 0.01 mm/s (Domain 2) (The location corresponds to the bottom region of the cup)

the cup and those examined at the radius and the inside wall regions are not any different, signifying microstructural homogeneity. However, the microstructure recorded in the outside rib region does not undergo significant change, compared with the starting as-cast

microstructure (Fig. 2). This is because the local strain in this region is too low to cause dynamic recrystallization. The microstructures clearly showed the occurrence of DRX and the average grain size obtained in Domain 1 (10 μm) is smaller than that in Domain 2 (22 μm).

The microstructures obtained at various locations of the forging conducted at 300 °C and 1 mm/s, which falls within the lower temperature instability regime of the processing map (Fig. 3), are shown in Fig. 7. The flow localization is clearly observed in the bottom, radius and inside-wall regions. In the outside wall region, the microstructure did not exhibit much change due to low local strain values. The microstructures obtained at similar locations on the forging conducted at 500 °C and 10 mm/s are shown in Fig. 8. The flow localization does not look very intense because of the changes that are caused by post-deformation cooling from the high temperature. Thus, the microstructural observations completely validate the workability regions where DRX occurs as well as the flow instability regions of the processing map.

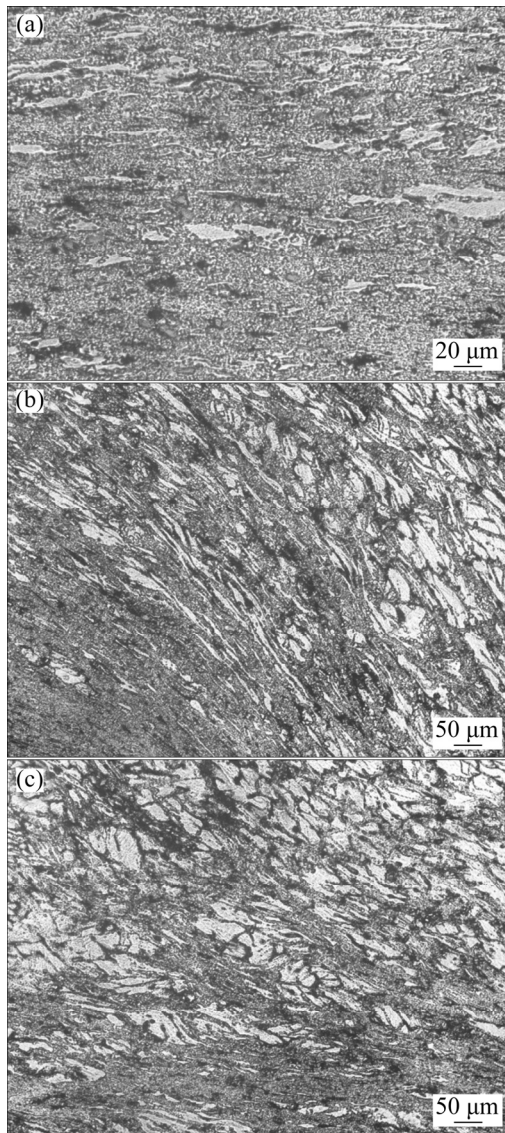


Fig. 7 Microstructures of Mg-4Al-2Ba-2Ca specimens forged at 300 °C, 1 mm/s (instability regime): (a) Bottom region; (b) Radius region; (c) Side-wall region

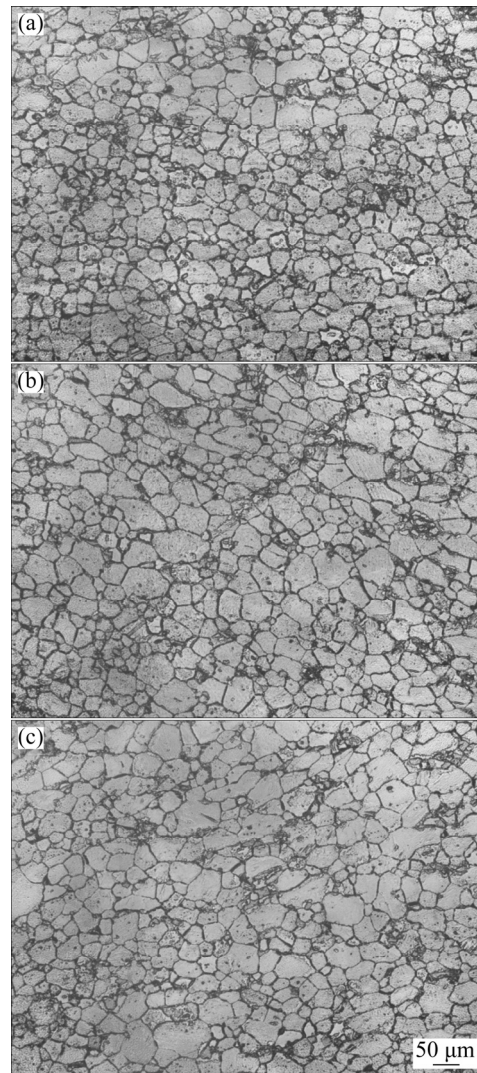


Fig. 8 Microstructures of Mg-4Al-2Ba-2Ca specimens forged at 500 °C, 10 mm/s (instability regime): (a) Bottom region; (b) Radius region; (c) Side-wall region

4.5 Load–stroke curves and shapes of forged specimens

The curves representing semi-close die forging involve three stages as follows: (1) increase in the load until plastic flow initialization, (2) material flow until the cup formation is complete, and (3) direct material compression in the bottom of the cup, resulting in a steep increase in the load with stroke.

The load–stroke curves recorded during the forging experiments at 300 °C, 340 °C (Domain 1), 460 °C (Domain 2), and 500 °C and at different forging speeds are shown in Fig. 9. The curves obtained at 300 °C (Fig. 9(a)) are uneven at all the forging speeds because the corresponding strain rates fall in the instability region of the map. When the temperature is increased to 340 °C (Fig. 9(b)), only the slowest speed (0.01 mm/s) is in the DRX domain, and the load–stroke curve is steady and as expected, while the curves are uneven at higher speeds. The curves obtained at 460 °C at all speeds are smooth

(Fig. 9(c)) because these curves are within DRX domain (Domain 2). Conversely, at 500 °C, the curve for the highest speed of 10 mm/s (Fig. 9(d)) is uneven because this curve is covered by the instability regime of the processing map.

The bottom views of ABAx422 forged specimens at different temperatures and forged speeds are shown in Fig. 10. Clearly, the specimens forged under conditions

corresponding to the two DRX domains: Domain 1, namely, 340 and 380 °C and a speed of 0.01mm/s (nearest to Domain 1) and Domain 2, namely 420, 460 and 500 °C and speeds of 0.01, 0.1 and 1.0 mm/s, possess the expected regular shapes for this component under good workability conditions. The specimens forged at 300 °C and 500 °C and the highest speed were fractured because of the flow instability.

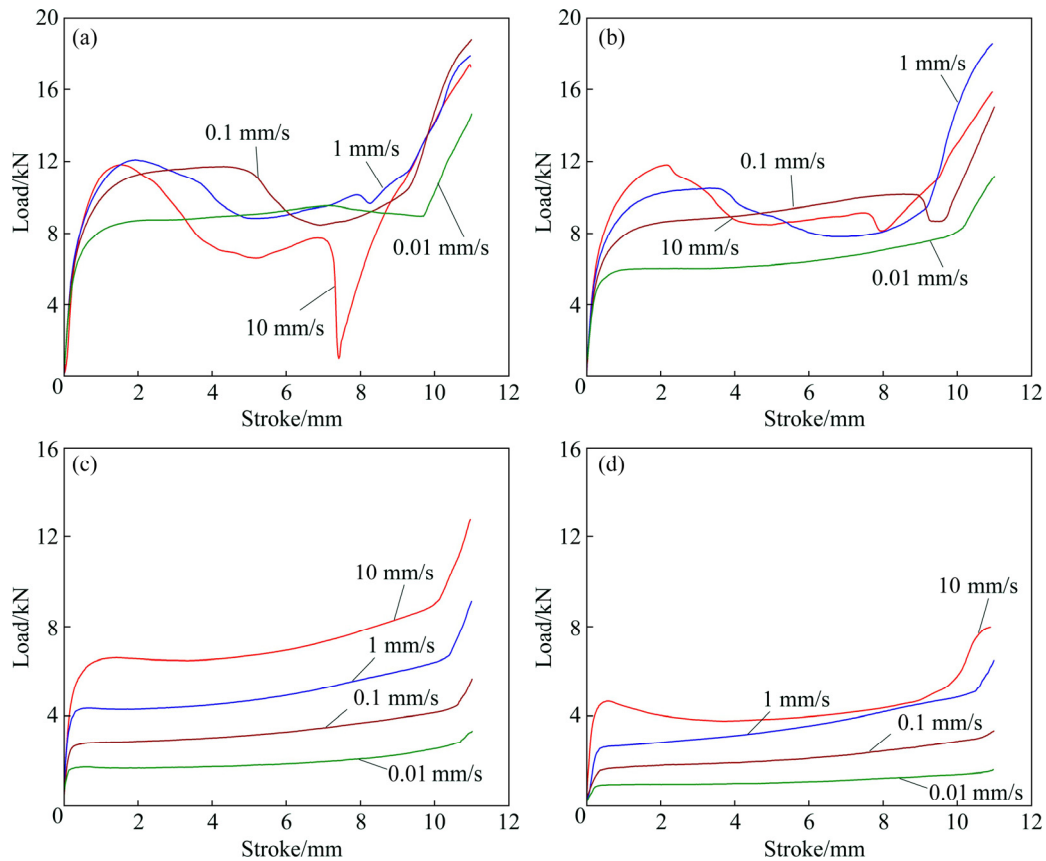


Fig. 9 Load–stroke curves obtained for forging of ABAx422 alloy at different speeds and temperatures: (a) 300 °C; (b) 340 °C; (c) 460 °C; (d) 500 °C

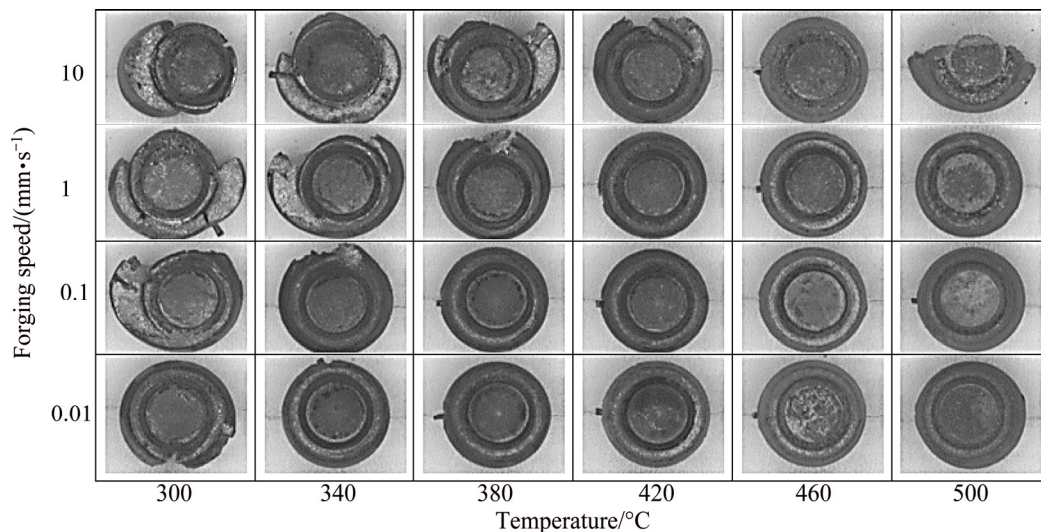


Fig. 10 Geometries of ABAx422 specimen forged at different temperatures and forging speeds (Bottom view)

Load–stroke curves obtained for forging simulations 340 °C, 0.01 mm/s (Domain 1) and 460 °C, 0.01 mm/s (Domain 2) are shown in Fig. 11 and compared with those obtained from forging experiments. A reasonable agreement exists between the simulated and experimental curves validating the simulation model. Simulation with a higher friction factor marginally changes the loads, indicating insignificant friction contribution.

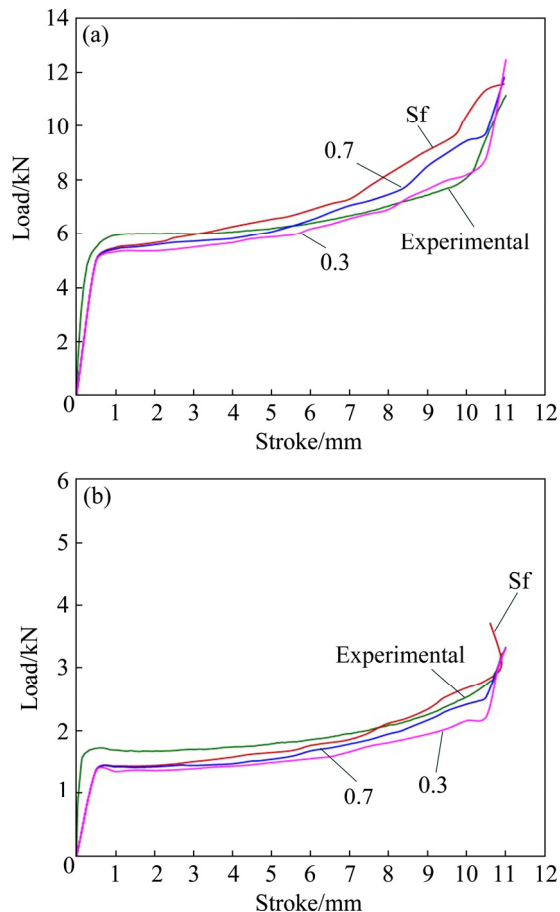


Fig. 11 Comparison of load–stroke curves obtained from finite element simulation for three friction factors (sticking friction (Sf), 0.7 and 0.3) and actual forging experiments: (a) 340 °C, 0.01 mm/s (Domain 1); (b) 460 °C, 0.01 mm/s (Domain 2)

5 Conclusions

1) Processing map exhibits two domains within the following temperature and strain rate ranges: (1) 300–390 °C and 0.0003–0.001 s⁻¹, and (2) 400–500 °C and 0.0003–0.3 s⁻¹, both of which show the occurrence of DRX.

2) Finite element simulation of a rib-web (cup-shaped) forging in ABaX422 alloy conducted in the DRX domains accurately predicts load–stroke curves that correlate well with experimental data. The load–stroke curves obtained for forgings done under conditions in the flow instability regimes of the map are

uneven, unlike those obtained when being forged in the DRX domains.

3) The microstructures obtained in the components forged under conditions in Domain 1 and Domain 2 of the processing map exhibit DRX, and validate the processing map predictions that the grain size in Domain 1 is finer than in Domain 2. Forging in the regimes of flow instability of the processing map results in flow localization in the microstructure and disintegration of specimens before the final shape is forged.

Acknowledgements

This work has been fully supported by Strategic Research Grant (Project #7002744) from the City University of Hong Kong, China.

References

- [1] PEKGULERYUZ M, CELIKIN M. Creep resistance in magnesium alloys [J]. *International Materials Reviews*, 2010, 55: 197–217.
- [2] HAN Q, KAD B K, VISWANATHAN S. Design perspectives for creep-resistant magnesium die-casting alloys [J]. *Philosophical Magazine*, 2004, 84: 3843–3860.
- [3] DIERINGA H, HORT N, KAINER K U. Barium as alloying element for a creep resistant magnesium alloy [C]//KAINER K U. *Magnesium: 8th International Conference on Magnesium Alloys and their Applications 2009*. Weimar, Germany: 2009: 62–67.
- [4] HU Guang-shan, ZHANG Ding-fei, DONG Yu-feng, CHEN Xia, JIANG Lu-yao, PAN Fu-cheng. Microstructures and mechanical properties of as-extruded and heat treated Mg–6Zn–1Mn–4Sn–1.5Nd alloy [J]. *Transactions of Nonferrous Metals Society of China*, 2015, 25: 1439–1445.
- [5] SUN Cui-cui, LIU Ke, WANG Zhao-hui, LI Shu-bo, DU Xian, DU Wen-bo. Hot deformation behaviors and processing maps of Mg–Zn–Er alloys based on Gleeble–1500 hot compression simulation [J]. *Transactions of Nonferrous Metals Society of China*, 2016, 26: 3123–3124.
- [6] ABU LEIL T, HORT N, DIERINGA H, BLAWERT C, HUANG Y, KAINER K U, RAO K P. Development and characterization of a series of Mg–Sn–Ca alloys [C]//PEKGULERYUZ M O, MACKENZIE L W F. *Magnesium Technology in Global Age*. Montreal, Canada: Canadian Institute of Mining, Metallurgy and Petroleum, 2006: 739–749.
- [7] BRONFIN B, MOSCOVITCH N, TROSTENETSKY V, GERZGBERG G, NAGAR N, YEHUDA R. High performance HPDC alloys as replacements for A380 aluminum alloy [C]//PEKGULERYUZ M O, NEELAMEGGHAM N R, BEALS R S. *Magnesium Technology 2008*. Warrendale, PA: TMS, 2008: 411–415.
- [8] WANG Z, GENG H, LI J, TENG X. Influence of Y and Ba on microstructure and mechanical properties of AZ91 magnesium alloys, [J]. *Key Engineering Materials*, 2007, 353–358: 1593–1596.
- [9] JING B, YANGSHAN S, SHAN X, FENG X, TIANBAI Z. Microstructure and tensile creep behavior of Mg–4Al based magnesium alloys with alkaline-earth elements Sr and Ca additions [J]. *Materials Science and Engineering A*, 2006, 419: 181–188.
- [10] ABU LEIL T, RAO K P, HORT N, KAINER K U. Corrosion behavior and microstructure of a broad range of Mg–Sn–X alloys [C]//LUO A A, NEELAMEGGHAM N R, BEALS R S. *Magnesium Technology 2006*. Warrendale, PA: TMS, 2006: 281–286.
- [11] TSUKEDA T, UCHIDA R, SAITO K, SUZUKI M, KOIKE J,

- MARUYAMA K, KUBO H. Effects of alloying elements of the creep resistance of thixomolded Mg–Al–Ca–X (X=Si, Zn, Mn, Ba, Sr) alloys [C]//KAINER K U. Magnesium Alloys and their Applications. Weinheim: Wiley-VCH Verlag GmbH, 2006: 47–52.
- [12] RAO K P, IP H Y, SURESH K, PRASAD Y V R K, WU C M L, HORT N, KAINER K U. Compressive strength and hot deformation mechanisms in as-cast Mg–4Al–2Ba–2Ca (ABaX422) alloy [J]. Philosophical Magazine, 2013, 93: 4364–4377.
- [13] SASTRY D H, PRASAD Y V R K, VASU K I. On the stacking fault energy of some close packed hexagonal metals [J]. Scripta Metallurgica, 1969, 3: 927–929.
- [14] MORRIS J R, SCHARFF J, HO K M, TURNER D E, YE Y Y, YOO M H. Prediction of a $\{11\bar{2}\}$ hcp stacking fault using a modified generalized stacking fault calculation [J]. Philosophical Magazine A, 1997, 76: 1065–1077.
- [15] RAO K P, PRASAD Y V R K. Materials modeling and finite element simulation of isothermal forging of electrolytic copper [J]. Materials and Design, 2011, 32: 1851–1858.
- [16] RAO K P, PRASAD Y V R K, SURESH K. Anisotropy of flow during isothermal forging of rolled AZ31B magnesium alloy plate in three orthogonal directions: Correlation with processing maps [J]. Materials Science and Engineering A, 2012, 558: 30–38.
- [17] RAO K P, PRASAD Y V R K, SURESH K. Anisotropy of flow during forging of rolled AZ31B plate in transverse direction: Validation of Materials Models [J]. Materials Science Forum, 2011, 690: 57–60.
- [18] RAO K P, PRASAD Y V R K, SURESH K. Materials modeling and simulation of isothermal forging of rolled AZ31 magnesium alloy: Anisotropy of flow [J]. Materials and Design, 2011, 32: 2545–2553.
- [19] PRASAD Y V R K, RAO K P, SASIDHARA S. Hot working guide: A compendium of processing maps [M]. 2nd ed. Materials Park, OH: ASM International, 2015.
- [20] PRASAD Y V R K, SESHACHARYULU T. Modeling of hot deformation for microstructural control [J]. International Materials Reviews, 1998, 44: 243–258.
- [21] ZIEGLER Z. Some extremum principles in irreversible thermodynamics with applications to continuum mechanics [C]//SNEDDON I N, HILL R. Progress in Solid Mechanics. Volume 4. New York: John Wiley, 1965: 91–193.
- [22] KOBAYASHI S, OH S I, ALTAN T. Metal forming and the finite-element method [M]. Oxford and New York: Oxford University Press, 1989: 1–41.
- [23] OH S I. Finite element analysis of metal forming processes with arbitrarily shaped dies [J]. International Journal of Mechanical Sciences, 1982, 24: 479–493.
- [24] SURESH K, RAO K P, PRASAD Y V R K, HORT N, KAINER K U. Microstructure and mechanical properties of as-cast Mg–Sn–Ca alloys and effect of alloying elements [J]. Transactions of Nonferrous Metals Society of China, 2013, 23: 3604–3610.
- [25] SURESH K, RAO K P, PRASAD Y V R K, WU L C M, HORT N, DIERINGA H. Mechanism of dynamic recrystallization and evolution of texture during hot working of Mg–4Al–2Ba–2Ca alloy [J]. Metals, 2017, 7(12): 539.
- [26] SIVAPRASAD P V, VENUGOPAL S, DAVIES C H J, PRASAD Y V R K. Identification of optimum process parameters for hot extrusion using finite element simulation and processing maps [J]. Modelling and Simulation in Materials Science and Engineering, 2004, 12: 285–291.
- [27] OU H, LAN J, ARMSTRONG C G, PRICE M A, WALLOE S J, WARD M J. Reduction in postforging errors for aerofoil forging using finite element simulation and optimization [J]. Modelling and Simulation in Materials Science and Engineering, 2006, 14: 179–193.
- [28] JIN Zhao-yang, LI Nan-nan, ZHANG Qi, YAN Kai, CUI Zhen-shan. Effects of forging parameters on uniformity in deformation and microstructure of AZ31B straight spur gear [J]. Transactions of Nonferrous Metals Society of China, 2017, 27: 2172–2180.

Mg–4Al–2Ba–2Ca (ABaX422)合金的热锻及热加工图的构建

K. SURESH¹, K. P. RAO¹, Y. V. R. K. PRASAD², N. HORT³, H. DIERINGA³

1. Department of Mechanical and Biomedical Engineering, City University of Hong Kong, Tat Chee Avenue, Kowloon, Hong Kong, China;
2. Processingmaps.com No. 2/B, Vinayaka Nagar, Hebbal, Bengaluru 560024, India;
3. Helmholtz-Zentrum Geesthacht, Institute of Materials Research, Magnesium Innovation Centre, Max-Planck-Straße 1, Geesthacht 21502, Germany

摘要: 将 Mg–4Al–2Ba–2Ca (ABaX422) 合金在 300~500 °C 的温度范围内、0.01~10 mm/s 的加工速率下热锻成杯型件, 构建其热加工图, 并研究其显微组织的演变。采用有限元法对该工艺进行模拟, 估计加工余量的局部应变速率和平均应变速率范围。热加工图存在以下 2 个区域: (1) 300~390 °C, 0.0003~0.001 s⁻¹; (2) 400~500 °C, 0.0003~0.3 s⁻¹; 这 2 个区域都存在动态再结晶(DRX)。该图表明, 在高应变速率和低于 400 °C 的温度下存在大范围的流动失稳区, 在此区域会发生流动局部化。在上述 2 个区域条件下制备的锻件完好且组织均匀, 在第一个区域条件下锻造所获锻件的晶粒尺寸更小。然而, 当在流动失稳区锻造时, 合金在最终成形前发生断裂。实验结果表明, 上述 2 个区域条件下的荷载–行程曲线与模拟曲线吻合较好, 而在失稳区获得的曲线则不平坦。

关键词: 镁合金; 加工图; 热锻; 动态再结晶